REGULAR PAPER • OPEN ACCESS

Laser-combined multiprobe microscopy and its application to the materials with atomic layer thickness

OPEN ACCESS

Japanese Journal of Applied Physics **61**, SL1011 (2022) **REGULAR PAPER**

https://doi.org/**10.35848/1347-4065/ac6a3c**

Laser-combined multiprobe microscopy and its application to the materials with atomic layer thickness

Hiroyuki Mogi[1], Zi-han Wang[1], Ibuki Kuroda[1], Yuhei Takaguchi[2], Yasumitsu Miyata[2], Atsushi Taninaka[1,3], Yusuke Arashida[1], Shoji Yoshida[1], Osamu Takeuchi[1], and Hidemi Shigekawa[1*]

[1]*Faculty of pure and applied sciences, University of Tsukuba, Tsukuba, Ibaraki 305-8573, Japan*
[2]*Department of Physics, Tokyo Metropolitan University, Hachioji, Tokyo 192-0397, Japan*
[3]*TAKANO Co., Ltd., Miyano-mura, Kamiina-gun, Nagano 399-4301, Japan*

[*]E-mail: hidemi@ims.tsukuba.ac.jp

Received January 31, 2022; revised April 1, 2022; accepted April 24, 2022; published online June 23, 2022

We have developed a method of evaluating the photo-induced carrier dynamics of nanostructures by combining optical technologies with multiprobe microscopy techniques. Using multiple probes, measurement can be carried out even for a small sample without complicated pretreatments, such as attaching electrode structures. Using transition metal dichalcogenides as a sample and a continuous laser or an ultrashort pulse laser as the light source, we demonstrated analyses of the carrier dynamics related to trap levels in a millisecond to second time domain and the ultrafast photoexcited carrier dynamics in the picosecond region. © 2022 The Author(s). Published on behalf of The Japan Society of Applied Physics by IOP Publishing Ltd

1. Introduction

The development of electronics to date has been promoted by the miniaturization of functional devices. Molecular/atomic-level devices are expected to be realized in the future. However, as the size of devices decreases, it becomes more important to control phenomena such as carrier scattering due to nanoscale crystal irregularities and atomic-scale impurities. Therefore, there has been a strong desire for the development of measurement methods that can locally evaluate these effects. Scanning tunneling microscopy (STM) is one of the promising candidates for this purpose. STM was developed by Binnig and Rohrer in 1982[1)] and has contributed to numerous achievements in nanoscale science. In STM, a very sharp tip is brought close (within about 1 nm) to the surface of a conductive material or atoms/molecules adsorbed on the surface. Then, by measuring the tunnel current flowing between the sample and the tip, atomic structures or local electronic states can be analyzed at the nanoscale. However, only physical information immediately below the tip can be obtained using an ordinary STM system with a single tip.

Therefore, multiprobe (MP) microscopy techniques were introduced,[2–7)] which can accurately control the positions of multiple probes on the μm- to -nm scale. For example, local in-plane electrical conduction, including anisotropy, can be directly measured. Furthermore, by combining MP microscopy with optical technologies, it becomes possible to investigate local photoinduced characteristics of materials.[5,8–10)] In particular, when an MP microscopy system is combined with a pump-probe method using an ultrashort pulse laser, time-resolved measurement is possible even in the fs region[8,11–15)] while maintaining the spatial resolution of STM. Therefore, laser-combined MP microscopy has become a particularly powerful measurement method for evaluating photoinduced properties in a wide range of time and space regions.[8)]

Layered materials such as transition metal dichalcogenides (TMDCs) have recently been attracting considerable attention.[16–18)] TMDCs are two-dimensional sheetlike materials having a structure in which transition metal atoms are sandwiched between chalcogen atoms (S, Se, Te). They have a wide range of functions due to the variety of choices of elements. For example, a TMDC which has a 2H structure with Mo or W as the transition metal is a semiconductor with a bandgap in the visible light region[19)] and a TMDC with Zr or Hf is a wide bandgap semiconductor.[20)] It has also been reported that Nb-containing TMDCs exhibit superconductivity.[21)] Besides, TMDC semiconductors with Mo or W have electron mobilities comparable to that of Si,[22,23)] their monolayer (ML) films have a direct-transition-type band structure and show a strong light–matter interaction. Accordingly, TMDC semiconductors are being actively studied for applications to logic electronic circuits and optoelectronics/photonics devices.

Here, using our developed laser-combined MP microscopy, the following three experiments were conducted on TMDC semiconductors with an atomic layer thickness: (i) transport characteristic evaluation using two probes, (ii) ms-scale trap capture/emission analysis using a continuous light source, and (iii) ps-scale dynamics evaluation with a femtosecond pulse laser.

2. Laser-combined multiprobe microscopy

Figure 1(a) shows the system we have developed. Four probes can be used in the ultrahigh vacuum chamber ($\sim 10^{-8}$ Pa). Each probe scanner can be equipped with an ordinary STM probe or a conductive AFM (cAFM) cantilever as a contact probe for the electrode. Using a cAFM probe for contact can minimize damage during the contact process, even for ultrathin film samples such as TMDC MLs. The probes and sample can be aligned by observing the optical microscope (resolution $\sim$1 μm), and repeated local conduction measurements can be performed on a small sample without the need to form electrodes by lithography. It is also possible to introduce liquid He into the cryotank and carry out an experiment in a low-temperature environment down to 10 K.

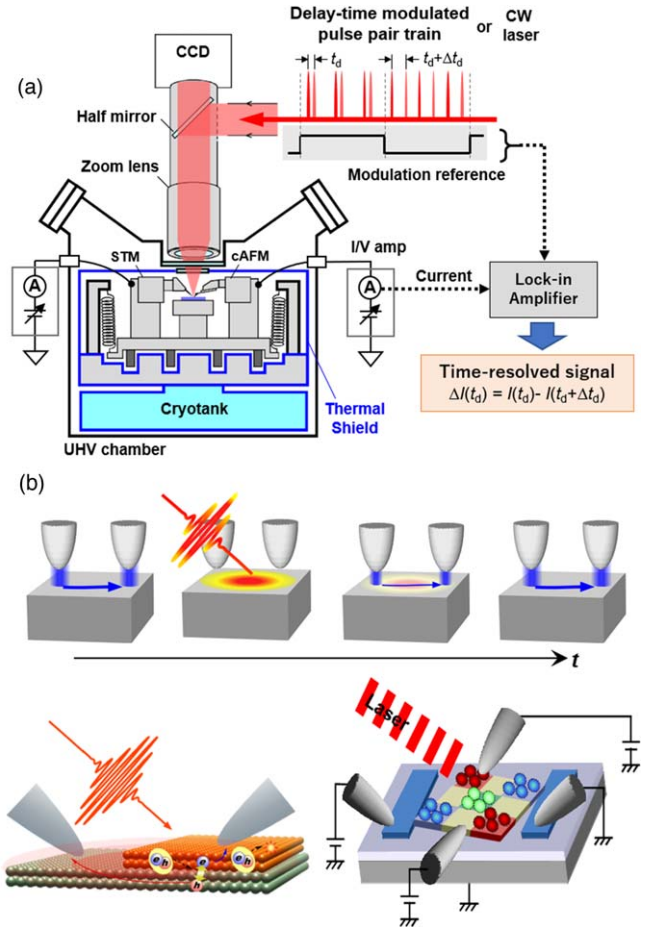

Fig. 1. (Color online) Time-resolved multiprobe STM system. (a) Schematic diagram of the system. t_d: delay time, Δt_d modulation width of delay time. (b) Examples of measurement using multiple probe system: (i) conduction dynamics (upper), (ii) carrier dynamics in TMDC (lower left), and (iii) carrier dynamics in nanostructures (lower right).

For photoexcitation, light beams are introduced and focused through the objective lens of the optical microscope. It is possible to irradiate any position without being hindered by the MP structures. If the probe/sample position fluctuates with respect to the light irradiation point, the effective light intensity at the measurement point will change, making the use of a vibration isolation system important. The eddy current damper in the chamber and the active air spring system enable stable measurements. A continuous light laser that can be electrically turned on and off or an ultrashort pulse laser with the modulation system we developed[8] was used as the light source in this study. By combining these laser systems with the MP system, the measurement of local photoinduced dynamics under operating conditions was realized. Examples of experimental setups are shown in Fig. 1(b). In this work, all probes were used in contact with the sample.

3. Evaluation of transport characteristics using multiple probes

Back-gated FET (BG-FET) structures have been used to investigate the carrier transport characteristics of low-dimensional semiconductors/semimetals of interest.[24,25] A general structure is a three-terminal device in which a channel material is placed on a substrate such as SiO_2/Si, and fixed electrodes are formed using a lithography process. However, since various chemical treatments are performed using a resist mask and a solvent in the lithography processes, some residues remain on the sample surface. Such residues greatly affect the conduction characteristics of low-dimensional semiconductors. Also, the spatial resolution of the analysis using the system is limited.

On the other hand, in measurements using MP techniques, some of the probes can be used to contact the sample without the need to form fixed electrodes. This has the advantage that no pretreatments are required and that the conduction characteristics can be measured while freely changing the electrode positions. Furthermore, the spatial resolution is in the nanoscale range.

Figures 2(a) and 2(b) show the sample and experimental setup used in our study, respectively. As shown in the optical microscopy image in Fig. 2(a), a ML/bilayer (BL) WSe_2 film grown by chemical vapor deposition (CVD) on a SiO_2/Si substrate[26] was used for the sample. A cAFM cantilever (spring constant 0.2 N m^{-1}, $PtIr_5$ coating) was placed in contact with the sample. It has been reported that when an electrode is placed on WSe_2 channel, the structure becomes a Schottky-type FET.[27,28] Information on Schottky barriers and carrier densities can be obtained by measuring the gate voltage (V_{gs}) dependence of the drain-source current (I_{ds}). As shown in Fig. 2(b), the position of the source probe was fixed, and the I_{ds} image was measured while scanning the position of the drain probe across the ML/BL interface. The red cross in Fig. 2(a) shows the source probe position, and the drain probe was scanned for measurement in the red point indicated by the red arrow.

Figure 2(c) shows the I_{ds} (current between source and drain) image obtained in the red square point in Fig. 2(a) under the conditions of $V_{gs} = 50$ V and $V_{ds} = 9$ V, where V_{gs} is the gate voltage applied between the gate and the source, and V_{ds} is the bias voltage applied between the drain and the source. A discontinuous change in current was clearly observed at the ML/BL interface. To analyze this characteristic in more detail, we stopped the scan every 120 nm while scanning the same area and swept the gate voltage V_{gs} from -80 V to $+80$ V to measure the current I_{ds} flowing between the source and the drain. Through the process, we obtained the I_{ds}–V_{gs} property. The typical I_{ds}–V_{gs} curves obtained in the ML and BL regions are shown in Fig. 2(d) on semi-logarithmic axes. The broken line in the figure shows the noise level of the current. Both graphs behave exponentially in the region of $V_{gs} = 0$–50 V. This indicates that the sample is an n-channel-type FET and that the main carriers are electrons. The slope of the semi-log plot is almost the same for the two curves, but the increase in V_{gs} in the ML region is shifted to the positive side by about 10 V from that in the BL region.

It has been reported that Schottky-type FETs exhibit exponential I_{ds}–V_{gs} characteristics when TMDC MLs of up to several layers are used as samples.[27,28] This could not be explained by the conventional model but is now understood to involve a mechanism that considers the effect of the electric field applied between the source and gate electrodes whereby electrons entering the channel from the electrode are

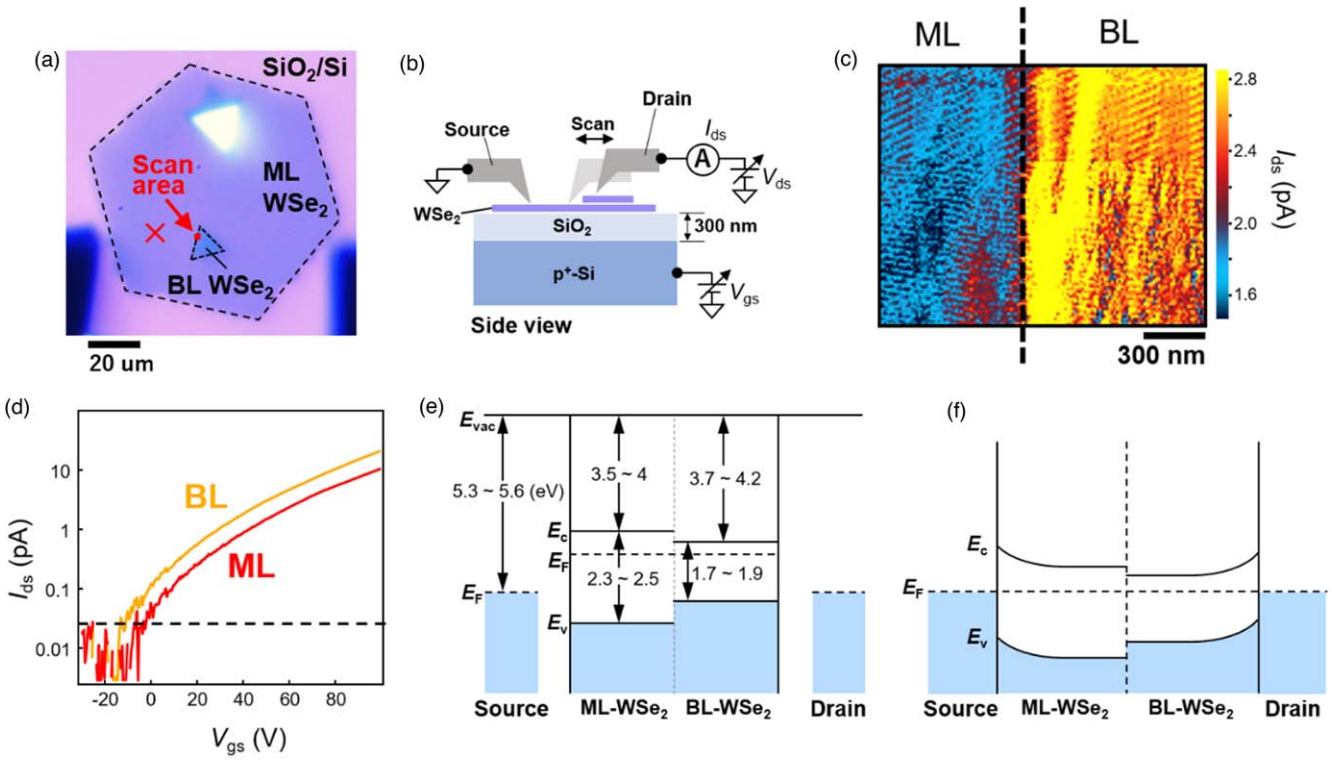

Fig. 2. (Color online) (a) Optical photograph of the sample. ML: monolayer, BL: bilayer. The red cross point is the source probe position, and the drain electrode probe was scanned in the red point indicated by the red arrow. (b) Schematic diagram of the experimental setup. (c) I_{ds} image obtained in the red square point in (a). (d) V_{gs} dependence of I_{ds} on ML and BL when irradiating the probe position on the source side. (e) Energy relationship between the probes and sample. (f) Band structure in the junction form.

produced by tunneling or thermal excitation above the Schottky barrier. This is consistent with our results as follows.

First, the bandgaps of ML and BL WSe_2 are about 2.4 eV and 1.8 eV, respectively, and the electronegativity of the BL is about 0.2 eV larger than that of the ML.[29] Therefore, the band structure when the probe is not in contact can be expressed as shown in Fig. 2(e). If the probe is placed in contact in this state, the Schottky barrier will be lower on the drain side than on the source side [Fig. 2(f)]. Thus, the rising voltage of the BL will become smaller than that of the ML because the electronegativity in the BL region is large, and the effective Schottky barrier is lowered accordingly. As shown in Fig. 2(d), the slope of the semi-log plot did not change and only a shift in V_{gs} that depended on the Schottky barrier height was observed, which is also consistent with the model.

We succeeded in showing that the change in characteristics caused by the differences in Schottky barrier height can be evaluated with nanoscale spatial resolution by MP-STM. It has thus become possible to evaluate the characteristics of FETs together with the information of local structures such as atomic-scale defects observed by STM.

4. Analysis of millisecond-range optical transient response

4.1. Examination of the measurement method

TMDCs have a strong light–matter interaction and exhibit up to 10% light absorption in their MLs. Therefore, TMDCs exhibit high responsivity when used as a photodetector as compared with three-dimensional (3D) semiconductors such as Si. On the other hand, the response time of Si is $\sim 10^{-8}$ s, whereas that of TMDC materials is 10^{-3}–10^{-1} s, and the gain bandwidth when TMDCs are used as a photodetector is almost the same as that of the conventional 3D semiconductors. The slow optical response of TMDC-based materials is due to the trap levels existing in the substrate and channels. Therefore, it is very important to analyze this response so that the performance of TMDCs can exceed that of conventional photodetectors. We attempted to develop a method of measuring the dynamics of the photoconductive response at the nanoscale using MP microscopy.

First, we carried out an experiment using the MP-STM system combined with a continuous light source to measure the ms-scale optical response. Figure 3(a) shows the measurement setup. After the two probes were brought in contact with any desired point on the sample, continuous light with on-off modulation was intermittently irradiated between the probes. The electrical connection was a BG-FET structure using two conductive AFM cantilevers, as in the case of Fig. 2. We introduced three laboratory-built preamplifiers for multiprobe measurement so that the currents flowing through the drain probe, source probe, and gate electrode could be detected independently. If there is a large difference in the response bands of the three preamplifiers, an artifact will occur when the difference in the time response of each preamplifier is taken. To avoid such a problem, the phase compensation capacitor of the current–voltage conversion circuit of each preamplifier was adjusted to make the response band uniform. From the step response time, it was confirmed that the band was $\sim$1 kHz. A semiconductor laser (wavelength 532 nm) that can be electrically switched on and

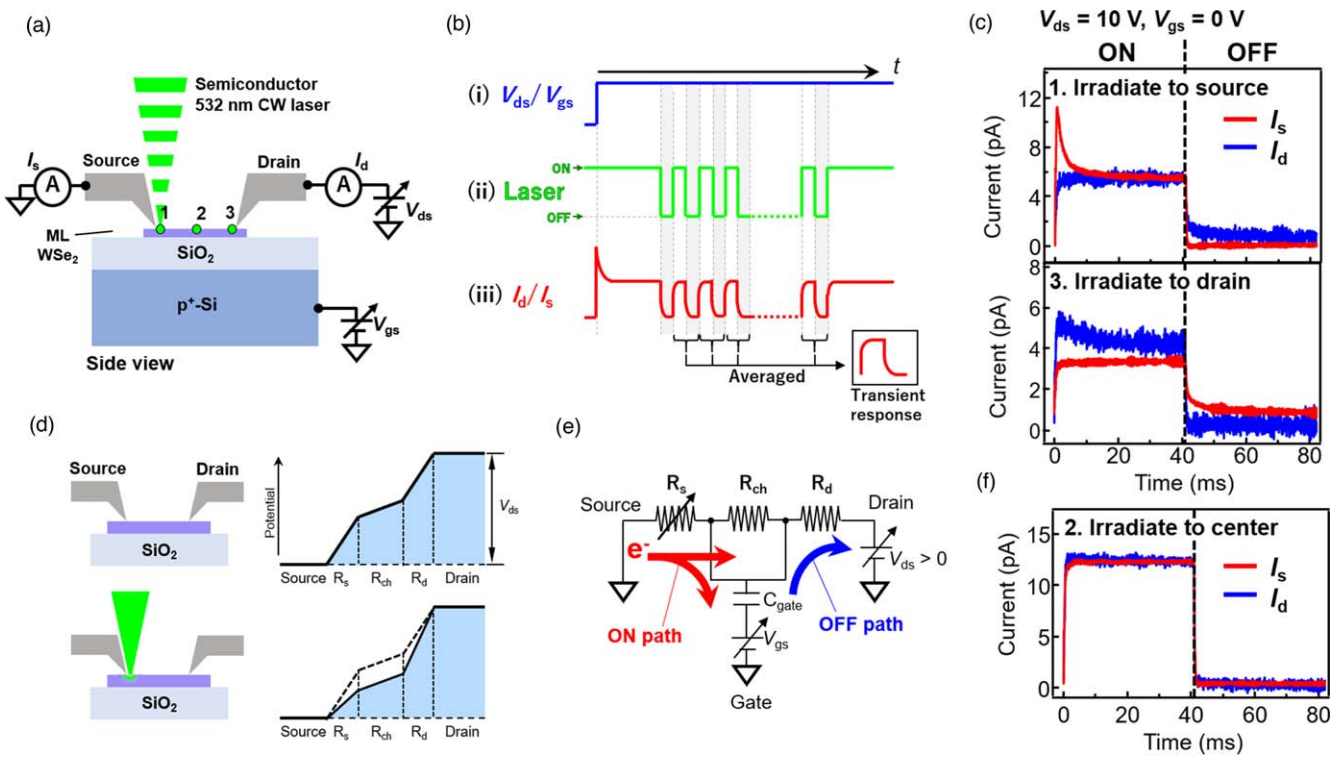

Fig. 3. (Color online) (a) Schematic diagram of the measurement setup. (b) Measurement sequence. (c) The light irradiation positions were set to 1 and 3 shown in (a). Measurement results of I_s and I_d transient responses with and without light irradiation. $V_{ds} = 10$ V, $V_{gs} = 0$ V. (d) Potential distribution between source and drain with and without light irradiation to position 1 shown in (a). (e) Circuit diagram corresponding to the configuration of the measuring unit. (f) Time dependences of I_d and I_s when the light irradiated to the center of the channel between the source and drain was turned on and off.

off was used as the light source. The analog modulation band of the light source was 250 kHz, which is sufficiently faster than the response of the preamplifier.

Figure 3(b) shows the measurement sequence of ms optical response dynamics. (i) First, V_{ds} or V_{gs} is changed to the set value. When V_{ds}/V_{gs} is changed, a pulse current flows to the parasitic capacitance of the system and the capacitance component of the sample. Thus, we must wait for a certain period until the current reaches a steady value. (ii) Next, measurements are carried out repeatedly to acquire the time response of I_{ds} while turning the light on and off at a regular interval. (iii) Thus, a transient response curve can be obtained by integrating and averaging the data. Then, returning to (i), V_{ds}/V_{gs} is changed to a different value and the measurement is repeated.

First, the transient optical response of ML-WSe_2 on a SiO_2/Si substrate prepared under the same conditions as the experiment shown in Fig. 2 was analyzed. Figure 3(c) shows the results when the light irradiation positions were set to 1 and 3 in Fig. 3(a). The experimental conditions were $V_{ds} = 10$ V, $V_{gs} = 0$ V, a drain-source probe distance of ~ 7 μm, light intensity = 0.5 mW, and a light spot diameter of ~ 2 μm. When the contact on the source side was irradiated, both currents, I_d and I_s, increased when the light was turned on, but a sharp peak occurred only in I_s. On the other hand, the opposite tendency was observed when the drain side was irradiated. The difference in noise level between I_d and I_s is due to the fact that no voltage was applied to the preamplifier measuring I_s, where no noise originated from the voltage source.

When the measurement is performed in a steady-state and there is no leakage current to the gate, I_d and I_s should be equivalent. However, as shown in Fig. 3(c), when the light was on, a pulselike current peak occurred in the probe near the light spot, whereas when the light was turned off, the current slowly decayed in the probe far from the light spot. The reason for the difference between I_d and I_s is considered to be the presence of capacitance components in the channel, which cause charging and discharging.

The origin of this phenomenon is considered to be the change in conductivity around the probe due to light irradiation. Figure 3(d) shows the in-plane potential distributions when a positive voltage is applied to the drain without (upper) and with light illumination at the source probe. A nonlinear potential distribution is formed in the two-dimensional channel, and a large potential gradient is generated in the vicinity of the probes. The resistances near the drain and source contacts are respectively written as R_d and R_s, and contact resistance is not considered for simplicity. When the vicinity of the source probe is irradiated, a large number of electron–hole pairs are generated. In this case, electrons flow to the channel side and holes flow to the source probe side owing to the in-plane electric field produced by V_{ds}. In addition, screening occurs in the irradiation spot, and the resistance R_s near the probe decreases owing to the increase in carrier density. As a result, the voltage drop near the source probe decreases, and the potential of the entire channel drops [Fig. 3(d), lower figure]. Thereby, the potential difference between the gate and the channel also changes, and the capacitance between the gate and the source is charged so

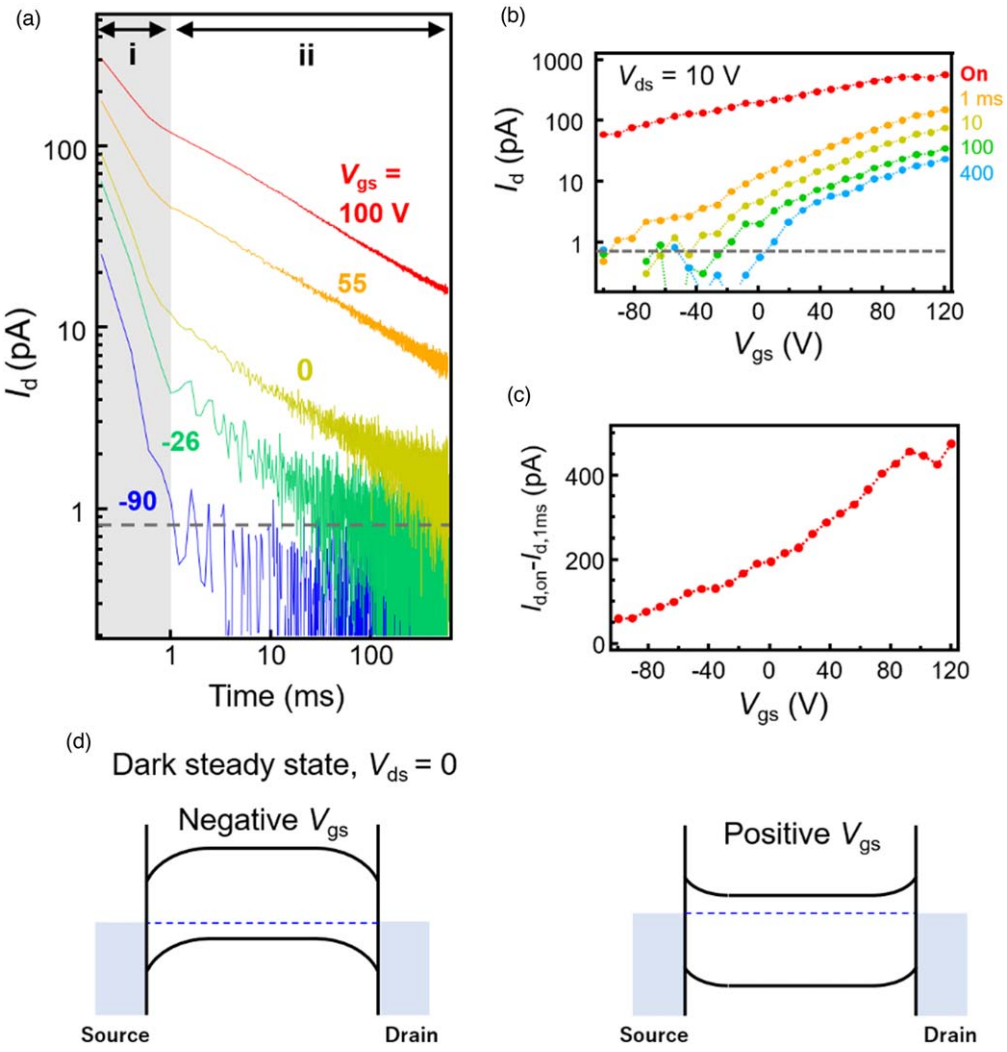

Fig. 4. (Color online) (a) Time dependence of I_d after light irradiation was stopped. (b) V_{gs} dependence of I_d at the time of light irradiation and I_d at each time after stopping light irradiation. (c) V_{gs} dependence of I_s–I_d obtained by subtracting the I_d after 1 ms from that immediately after light irradiation was stopped. (d) Band structures when V_{gs} is negative (left) and positive (right) with $V_{ds} = 0$.

that a peak displacement current is generated from the source probe side with low resistance. When the light is turned off, the potential distribution returns to that before light irradiation, but I_d slowly decreases because the charged electrons are extracted from the drain side.

Figure 3(e) shows a simple equivalent circuit and the electron path. The difference in transient response time constant when the source and drain sides were irradiated with light, shown in Fig. 3(c), is considered to be due to the difference in contact resistance. Namely, the RC coupling time constant increased owing to the large contact resistance of the drain probe.

Figure 3(f) shows the results obtained when the center of the channel between the probes was irradiated. The currents I_d and I_s are almost the same, which means that when the center of the channel is irradiated, the potential of the entire channel does not change owing to the effect mentioned above, and the effect of the displacement current due to capacitive coupling can be minimized. Therefore, to correctly evaluate the photoconductive response in the photoexcited multiprobe system, it is necessary to perform photoexcitation symmetrically with regard to the probe arrangement. This relationship holds even when the width of the light spot is large compared with the distance between the probes, provided that the light excitation is carried out uniformly on both probes. Thus, by reducing the distance between the probes to the nm scale, it is possible to measure the light conduction response more locally.

4.2. Application of the developed method

Next, keeping the photoirradiation at the central part between the probes, transient responses in I_d and I_s were measured while changing V_{gs}. The light intensity was 10 μW with $V_{ds} = 10$ V. The transient response up to 600 ms was measured at a sampling rate of 5 kHz after photoirradiation was stopped at 0 ms. Figure 4(a) shows a typical result. Figure 4(b) shows plots of I_d as a function of time for various V_{gs} values, which were obtained from all the measured data shown in Fig. 4(a). V_{gs} was changed within the range possible in this experiment. When V_{gs} higher than this range was applied, current leakage occurred and the sample was destroyed. As shown in Fig. 4(a), two different features with different slopes were observed in regions (i) $t < 1$ ms and (ii) $t > 1$ ms.

First, we consider the dynamics observed for (i) $t < 1$ ms. For ML-WSe_2, it has been reported that optical carrier

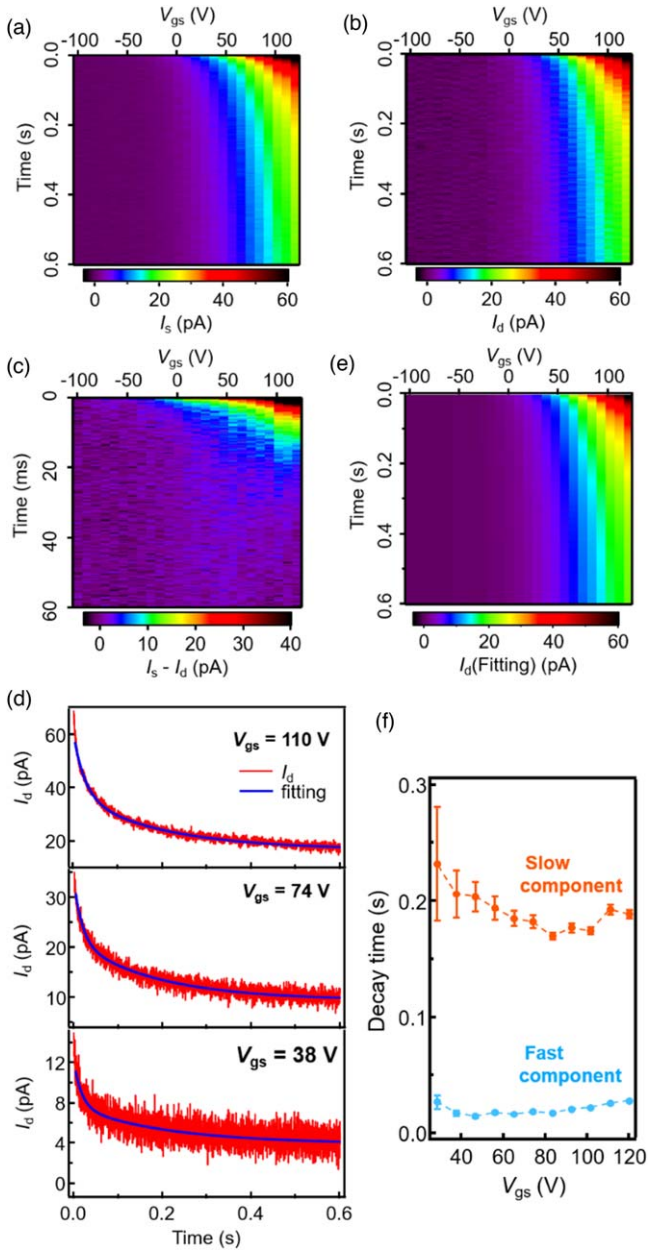

Fig. 5. (Color online) V_{gs} dependences of the (a) drain current I_d, (b) source current I_s, and (c) the difference between them I_s–I_d on the gate voltage and time. (d) Time-resolved spectra of I_d at $V_{gs} = +38$ V, $+60$ V, and $+100$ V, where the red lines are the experimental values and the solid blue lines are the fitting curves. (e) Fitting curves as a function of V_{gs}, with the intensity shown by the color scale. All time-resolved data were used. (f) V_{gs} dependence of the lifetimes of the two components.

recombination occurs on a time scale of ps to ns. Therefore, the 1 kHz band of the preamplifier used is considerably slower than the carrier recombination dynamics and all excited carriers were already recombined 1 ms after the illumination was turned off. Therefore, to examine in detail the photoexcited carriers $I_{d,on}$–$I_{d,1ms}$, the drain current $I_{d,1ms}$ measured 1 ms after the light was turned off was subtracted from the drain current $I_{d,on}$ measured during light irradiation for all the data similar to those in Fig. 4(b). The results are shown in Fig. 4(c). $I_{d,on}$–$I_{d,\ 1ms}$ increased as V_{gs} became increasingly positive. From the I_{ds}–V_{gs} characteristics in the dark state, as shown in Figs. 2(d) and 2(e), this sample is slightly of the n-type for $V_{gs} = 0$ V, and the Fermi level E_F is close to the conduction band. In the V_{gs} range of this experiment, the amount of electron doping increases as V_{gs} becomes increasingly positive. It has been reported that electrical doping reduces the binding energy of excitons in a $ReSe_2$ sample formed on graphene.[30] Figure 4(d) shows schematics of the band structures for positive and negative gate voltages under the dark condition. For simplicity, the trap levels are not shown here. Band bending due to the Schottky junction appears between the electrodes and the sample, and the sign of the gate voltage changes the direction of the electric field.[31] Therefore, when the number of free electrons increases with V_{gs} in the positive region, the screening is considered to weaken the Coulomb binding force of excitons. This effect should also be reflected in the change in the intensity of the photocurrent response to V_{gs} in region (i) of Fig. 4(a).

Next, we consider the dynamics in (ii) $t > 1$ ms. Photoexcited free carriers have already disappeared at $t = 1$ ms, and the emission of carriers captured by the trap levels immediately after the light has been turned off determines the subsequent dynamics of the current response. Such responses have been analyzed by macroscopic measurement methods such as deep-level transient spectroscopy[32] and photoinduced current transient spectroscopy[33] and other related techniques. Defect levels have been evaluated using these methods, and the large variation in response time for photoelectric devices using MoS_2 is a major problem to be solved for their application.[17,34] If the multiprobe method can be used to investigate the transient response in time domain (ii), it is expected to become an important technology indispensable for device miniaturization and further performance improvement.

When photoexcitation is stopped, the excess electrons generated by photoexcitation are captured by the trap levels in the bandgap. It has been reported that carriers are emitted from the trap levels after turning off the light, and a long-lived response (ms-s) is observed.[17,34,35] Therefore, by measuring the V_{gs} dependence of the I_d and I_s dynamics, the characteristics of the trap levels in this system can be analyzed. Figures 5(a)–5(c) show the dependences of I_s, I_d, and the difference between them I_s–I_d on V_{gs} and time. The color scale represents the intensity of each current. As can be seen, there is a region where I_s–I_d has a measurable value, indicating that there are holes emitted from the trap levels in this region and that there is a transient response of the holes in addition to that of the electrons. The value decreases as V_{gs} decreases and falls below the noise level at $V_{gs} < -90$ V.

Figure 5(d) shows the spectra of I_d obtained at $V_{gs} = +38$ V, $+74$ V, and $+110$ V, where the solid blue lines are the fitting curves for the data shown in red. The fitting was performed using a two-component exponential function, and the agreement with the experimental results is very good. Figure 5(e) shows the fitting curves as a function of V_{gs}, with the intensity shown by the color scale. A graph similar to that shown in Fig. 5(b) was obtained. Figure 5(f) shows the V_{gs} dependence of the lifetimes of the two components. The variation in the small-V_{gs} region is attributed to the weak signal and the low signal-to-noise ratio, as shown in Fig. 5(d). The shorter lifetime ($\sim$20 ms) is that of the holes, and the longer one ($\sim$200 m) is that of the electrons. The slow component appears to become slightly longer with V_{gs}.

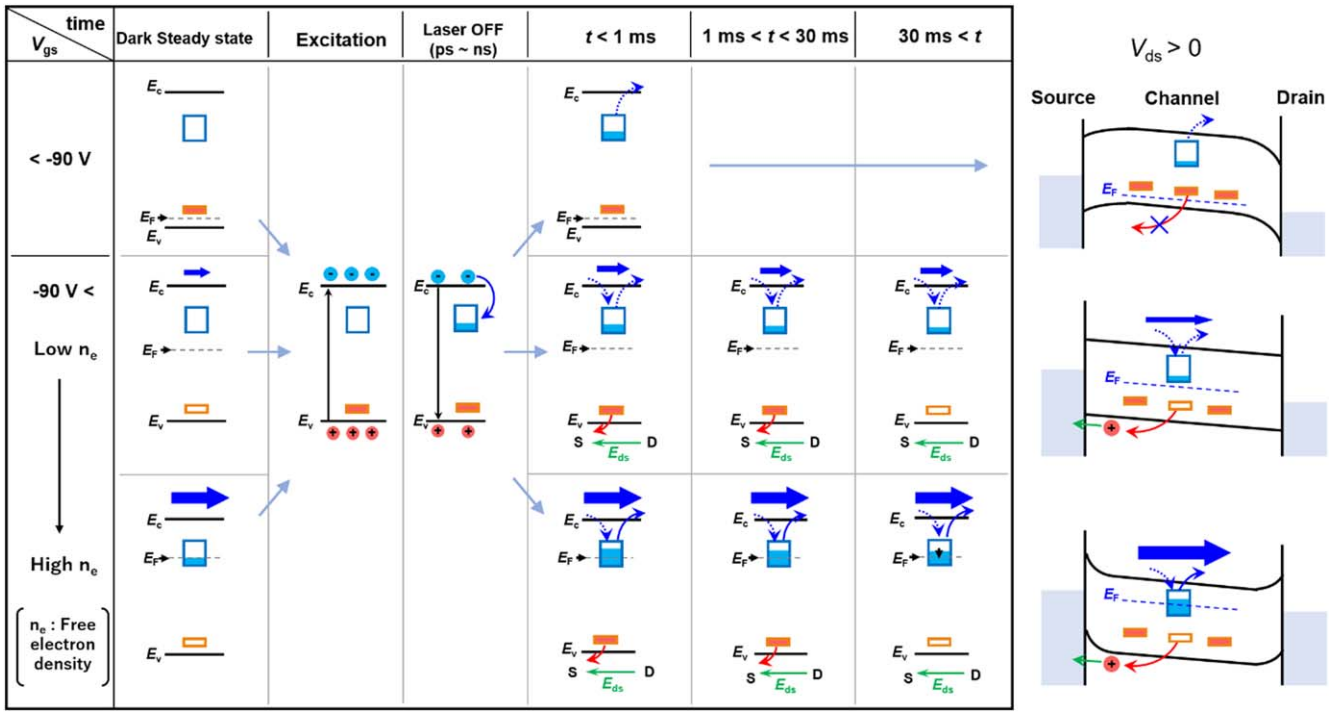

Fig. 6. (Color online) Model diagrams showing the time dependence of the band structures for different V_{gs} values. E_c: conduction band edge, E_F: Fermi energy, E_v: valence band edge, blue arrows: current flow, green arrows: electric field produced by V_{ds}, blue square: trap states for electrons, red square: trap states for holes, filled electrons/holes are shown by blue and red-colored regions. The schematics on the right show the band structures for different V_{ds} values.

Next, the results obtained for region (ii) shown in Fig. 4 are discussed. Figure 6 shows model diagrams of the time dependence of the band structures for different V_{gs} values. In accordance with the discussion thus, the time axis t is divided into the dark state, the excited state, and the time when excitation has stopped, i.e. $0 < t < 1$ ms, $1\text{ ms} < t < 30$ ms, and $30\text{ ms} < t$, respectively. The gate voltage is divided into $V_{gs} < -90$ V, where only the dynamics of photoexcited current is observed, and $-90\text{ V} < V_{gs}$, where the dynamics of holes and electrons captured at the trap levels are observed. The table on the left shows model diagrams of the carrier dynamics at trap levels under various conditions. The figures on the right show the change in band structure caused by V_{gs}.

At $V_{gs} < -90$ V, the Fermi level E_F is close to the valence band, and the trap levels at energies higher than E_f are empty, as shown in Fig. 6. Also, almost no steady current flows. The band is convex upwards. Therefore, the photoexcited electrons and holes reach the electrode and become the current observed in the region of $t < 1$ ms as shown in Fig. 4(a). Furthermore, no trapping occurs; thus, the carrier dynamics observed in region (ii) do not occur.

On the other hand, at $-90\text{ V} < V_{gs}$, the acceptor levels are filled with electrons under the dark condition. When the sample is photoexcited, the trap levels become empty, and when photoexcitation is stopped, the electrons in the valence band start to be trapped, thereby holes start to be emitted to the valence band. Then, the in-plane electric field drives the holes to the source electrode, causing the current dynamics of I_s–I_d, as shown in Fig. 5(c). The emission of electrons captured at the trap levels also occurs after the photoexcitation is stopped. A change in the number of electrons trapped in the trap levels affects the potential in the light spot area and mobility of electrons,[34,36] causing a change in steady current.[37,38] To provide a deeper and quantitative insight, it is necessary to evaluate the temperature dependence and other dependences. This is beyond the scope of this study and is left as a future task.

It has been shown that the laser-combined multiprobe system enables the analysis of the ms-scale photoinduced carrier dynamics related to trap levels. In low-dimensional semiconductor devices, the effect of trap levels existing at the surface and interface is large and there is a marked variation among samples, limiting the application of TMDCs.[17,34] Laser-combined MP-STM has enabled us to locally and repeatedly measure the photoconductive response without difficult pretreatments such as lithography, making it an effective analysis method for solving the above problems. Furthermore, by combining the method with the observation and imaging techniques of STM itself, it becomes possible to evaluate the dynamics of electronic states as compared with the nanoscale structures.

5. Evaluation of ps-scale carrier dynamics by time-resolved MP microscopy

Thus, we have evaluated the photoinduced conduction dynamics in the range of ms to s. Since carrier dynamics in the ultrahigh-speed region of low-dimensional materials are greatly affected by phenomena such as atomic-scale defects, the evaluation of the ultrafast carrier dynamics on the nm scale is also strongly required. Using the MP microscopy system, the probe position can be determined with nm accuracy, and it is possible to evaluate carrier dynamics in the ultrahigh-speed region even for a sample placed on an

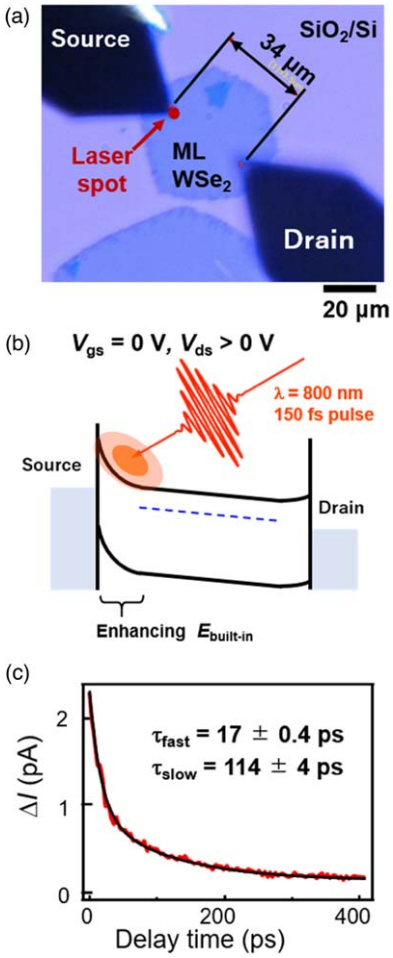

Fig. 7. (Color online) (a) Optical microscopy image of the measurement setup. (b) Schematic diagrams of the band structure under measurement condition. (c) Time-resolved signal obtained for CVD-grown ML WSe_2 on SiO_2/Si. The time-resolved signal in the range of 0–400 ps was fitted by a two-component exponential function.

insulating material. Thus, measurement results in the ms region have been shown, but here we show results obtained for the measurement of carrier dynamics in the ps region.

For CVD-grown ML WSe_2 on SiO_2/Si, the time-resolved measurement of the ps region was performed using the laser-combined MP-STM. Figure 7(a) shows an optical microscopy image of the measurement setup. Two cAFM cantilevers were brought into contact with the sample. The distance between the probes was set to 34 μm, and one of them was irradiated with a femtosecond laser pulse for measurement.

A delay time modulation method with pulse picking was used for the optical pump-probe system for time-resolved measurement.[8,12] The light source used was a Ti:sapphire laser with a wavelength of 800 nm, a pulse width of 150 fs, and an average intensity of ~30 mW. The voltages applied to the AFM probes were $V_{ds} = 20$ V and $V_{gs} = 0$ V. Figure 7(b) shows the band structure under the measurement condition.

Figure 7(b) shows the obtained time-resolved spectrum. The time-resolved signal in the range of 0–400 ps was fitted by a two-component exponential function. The early component was 17 ± 0.4 ps and the slow component was 114 ± 4 ps. Experiments using the conventional optical pump-probe method have already been reported, and the two lifetimes we obtained are in good agreement with the previous results.[39,40] The origin of the dynamics in the ps region is attributed to a mechanism involving very shallow trap levels[40] and Auger processes.[41] Using the laser-combined MP microscopy system we have developed, we demonstrated that time-resolved measurements at the ps level are possible.

6. Conclusion

By combining multiprobe microscopy techniques with optical measurement technology, we have realized a method of investigating the transient response of the electronic state of a sample to a light stimulus over a wide time range. Using STM, it is also possible to analyze the electronic state in comparison with the nanoscale structure. This method is expected to play an important role in developing new functional materials and devices in the future.

Acknowledgments

We acknowledge the financial support of a Grant-in-Aid for Scientific Research from Japan Society for the Promotion of Science and Japan (17H06088, 20H00341, 20H02605, 21H05232, 21H05234), and Japan Science and Technology Agency (JST) CREST program (JPMJCR1875, JPMJCR16F3).

1) G. Binnig, H. Rohrer, C. Gerber, and E. Weibel, Phys. Rev. Lett. **49**, 57 (1982).
2) H. Mogi, T. Bamba, M. Murakami, Y. Kawashima, M. Yoshimura, A. Taninaka, S. Yoshida, O. Takeuchi, H. Oigawa, and H. Shigekawa, ACS Appl. Electron. Mater. **1**, 1762 (2019).
3) S. Hasegawa, J. Phys.:Condens. Matter **31**, ab0bf4 (2019).
4) B. Voigtländer, V. Cherepanov, S. Korte, A. Leis, D. Cuma, S. Just, and F. Lüpke, Rev. Sci. Instrum. **89**, 101101 (2018).
5) T. Nakayama, O. Kubo, Y. Shingaya, S. Higuchi, T. Hasegawa, C. S. Jiang, T. Okuda, Y. Kuwahara, K. Takami, and M. Aono, Adv. Mater. **24**, 1675 (2012).
6) M. Hirose, E. Tsunemi, K. Kobayashi, and H. Yamada, Appl. Phys. Lett. **103**, 4 (2013).
7) M. Kolmer et al., Nat. Commun. **10**, 1573 (2019).
8) H. Mogi et al., Appl. Phys. Express **12**, 045002 (2019).
9) Y. Masaki, K. Tomita, Y. Kojima, and F. Kannari, Appl. Opt. **58**, 5595 (2019).
10) R. Fujimoto, A. Kaneta, K. Okamoto, M. Funato, and Y. Kawakami, Appl. Surf. Sci. **258**, 7372 (2012).
11) H. Mogi, Z. Wang, R. Kikuchi, C. Hyun Yoon, S. Yoshida, O. Takeuchi, and H. Shigekawa, Appl. Phys. Express **12**, 025005 (2019).
12) Y. Terada, S. Yoshida, O. Takeuchi, and H. Shigekawa, Nat. Photonics **4**, 869 (2010).
13) S. Yoshida, Y. Aizawa, Z.-H. Wang, R. Oshima, Y. Mera, E. Matsuyama, H. Oigawa, O. Takeuchi, and H. Shigekawa, Nat. Nanotechnol. **9**, 588 (2014).
14) S. Yoshida, Y. Arashida, H. Hirori, T. Tachizaki, A. Taninaka, H. Ueno, O. Takeuchi, and H. Shigekawa, ACS Photonics **8**, 315 (2021).
15) K. Yoshioka, I. Katayama, Y. Minami, M. Kitajima, S. Yoshida, H. Shigekawa, and J. Takeda, Nat. Photonics **10**, 762 (2016).
16) A. Castellanos-Gomez, Nat. Photonics **10**, 202 (2016).
17) G. Konstantatos, Nat. Commun. **9**, 5266 (2018).
18) D. Jariwala, V. K. Sangwan, L. J. Lauhon, T. J. Marks, and M. C. Hersam, ACS Nano **8**, 1102 (2014).
19) K. F. Mak, K. He, C. Lee, G. H. Lee, J. Hone, T. F. Heinz, and J. Shan, Nat. Mater. **12**, 207 (2013).
20) K. W. Lau, C. Cocchi, and C. Draxl, Phys. Rev. Mater. **3**, 074001 (2019).
21) H. Wang et al., Nat. Commun. **8**, 394 (2017).
22) W. Zhang, Z. Huang, W. Zhang, and Y. Li, Nano Res. **7**, 1731 (2014).
23) P. C. Shen et al., Nature **593**, 211 (2021).
24) K. S. Novoselov, A. K. Geim, S. V. Morozov, D. Jiang, Y. Zhang, S. V. Dubonos, I. V. Grigorieva, and A. A. Firsov, Science **306**, 666 (2004).

25) B. Radisavljevic, A. Radenovic, J. Brivio, V. Giacometti, and A. Kis, Nat. Nanotechnol. **6**, 147 (2011).
26) S. Li, S. Wang, D. M. Tang, W. Zhao, H. Xu, L. Chu, Y. Bando, D. Golberg, and G. Eda, Appl. Mater. Today **1**, 60 (2015).
27) A. Prakash, H. Ilatikhameneh, P. Wu, and J. Appenzeller, Sci. Rep. **7**, 12596 (2017).
28) W. Liu, J. Kang, D. Sarkar, Y. Khatami, D. Jena, and K. Banerjee, Nano Lett. **13**, 1983 (2013).
29) H. J. Liu, L. Jiao, L. Xie, F. Yang, J. L. Chen, W. K. Ho, C. L. Gao, J. F. Jia, X. D. Cui, and M. H. Xie, 2D Mater. **2**, 034004 (2015).
30) Z. Qiu et al., Sci. Adv. **5**, eaaw2347 (2019).
31) Y. Yi, C. Wu, H. Liu, J. Zeng, H. He, and J. Wang, Nanoscale **7**, 15711 (2015).
32) D. V. Lang, J. Appl. Phys. **45**, 3023 (1974).
33) C. Hurtes, M. Boulou, A. Mitonneau, and D. Bois, Appl. Phys. Lett. **32**, 821 (1978).
34) M. M. Furchi, D. K. Polyushkin, A. Pospischil, and T. Mueller, Nano Lett. **14**, 6165 (2014).
35) D. Kufer and G. Konstantatos, Nano Lett. **15**, 7307 (2015).
36) D. Knipp, R. A. Street, A. Völkel, and J. Ho, J. Appl. Phys. **93**, 347 (2003).
37) T. J. Echtermeyer et al., Nano Lett. **14**, 3733 (2014).
38) H. Huang et al., Nanotechnology **27**, 445201 (2016).
39) T. Godde et al., Phys. Rev. B **94**, 165301 (2016).
40) L. Li and E. A. Carter, J. Am. Chem. Soc. **141**, 10451 (2019).
41) Y. Li et al., Nanoscale **10**, 17585 (2018).